

Article

Machine Learning of Multi-Modal Tumor Imaging Reveals Trajectories of Response to Precision Treatment

Nesrin Mansouri ¹, Daniel Balvay ¹, Omar Zenteno ¹, Caterina Facchin ^{1,2}, Thulaciga Yoganathan ¹, Thomas Viel ¹, Joaquin Lopez Herraiz ³, Bertrand Tavitian ^{1,4,*,†} and Mailyn Pérez-Liva ^{1,3,*,†}

¹ INSERM, PARCC, Université Paris Cité, F-75015 Paris, France

² Cancer Drug Research Laboratory, Department of Medicine, Division of Medical Oncology, The Research Institute of the McGill University Health Center (RI-MUHC), Montréal, QC H4A 3J1, Canada

³ Nuclear Physics Group and IPARCOS, Department of Structure of Matter, Thermal Physics and Electronics, CEI Moncloa, Universidad Complutense de Madrid, 28040 Madrid, Spain

⁴ Radiology Department, AP-HP, European Hospital Georges Pompidou, F-75015 Paris, France

* Correspondence: bertrand.tavitian@inserm.fr (B.T.); m.perez.liva@fis.ucm.es (M.P.-L.);
Tel.: +33-153-98-80-54 (B.T.); +34-913-944-775 (M.P.-L.)

† These authors supervised this work and share the last position.

Simple Summary: In order to evaluate precision cancer therapies, it would be advantageous to measure at the same time their action on tumor growth and on the biological target of the therapy. New non-invasive hybrid imaging techniques allow access to multiple quantitative parameters. Here, we trained machine learning classifiers of features extracted from longitudinal in vivo co-registered metabolic, vascular and anatomical images in a mouse model of paraganglioma. We show that machine learning identifies ensembles of tumor states that correspond to stages of tumor evolution with or without anti-angiogenic treatment. These classifiers define individual trajectories of tumor progression and response to treatment, supporting the use of machine learning analysis of multiparametric imaging for the identification of response to anti-angiogenic treatment in this rodent model.



Citation: Mansouri, N.; Balvay, D.; Zenteno, O.; Facchin, C.; Yoganathan, T.; Viel, T.; Herraiz, J.L.; Tavitian, B.; Pérez-Liva, M. Machine Learning of Multi-Modal Tumor Imaging Reveals Trajectories of Response to Precision Treatment. *Cancers* **2023**, *15*, 1751. <https://doi.org/10.3390/cancers15061751>

Academic Editors: Jean-Emmanuel Bibault and Lei Xing

Received: 30 January 2023

Revised: 3 March 2023

Accepted: 8 March 2023

Published: 14 March 2023



Copyright: © 2023 by the authors. Licensee MDPI, Basel, Switzerland. This article is an open access article distributed under the terms and conditions of the Creative Commons Attribution (CC BY) license (<https://creativecommons.org/licenses/by/4.0/>).

Abstract: The standard assessment of response to cancer treatments is based on gross tumor characteristics, such as tumor size or glycolysis, which provide very indirect information about the effect of precision treatments on the pharmacological targets of tumors. Several advanced imaging modalities allow for the visualization of targeted tumor hallmarks. Descriptors extracted from these images can help establishing new classifications of precision treatment response. We propose a machine learning (ML) framework to analyze metabolic–anatomical–vascular imaging features from positron emission tomography, ultrafast Doppler, and computed tomography in a mouse model of paraganglioma undergoing anti-angiogenic treatment with sunitinib. Imaging features from the follow-up of sunitinib-treated ($n = 8$, imaged once-per-week/6-weeks) and sham-treated ($n = 8$, imaged once-per-week/3-weeks) mice groups were dimensionally reduced and analyzed with hierarchical clustering Analysis (HCA). The classes extracted from HCA were used with 10 ML classifiers to find a generalized tumor stage prediction model, which was validated with an independent dataset of sunitinib-treated mice. HCA provided three stages of treatment response that were validated using the best-performing ML classifier. The Gaussian naive Bayes classifier showed the best performance, with a training accuracy of 98.7 and an average area under curve of 100. Our results show that metabolic–anatomical–vascular markers allow defining treatment response trajectories that reflect the efficacy of an anti-angiogenic drug on the tumor target hallmark.

Keywords: multi-modal imaging; paraganglioma; machine learning; hierarchical clustering; treatment response

1. Introduction

Establishing treatment response is a crucial aspect of precision oncology [1]. This determination involves categorizing the patient's status into predefined discrete classes [2,3]. These classes are established by pooled assessment of the margins of variation of descriptive features extracted from medical data or images. Given the wide existing variety of medical data, imaging systems, and clinical protocols in oncology, there are standardized recommendations for defining treatment response. The World Health Organization (WHO) in 1979 determined four categories of response or non-response to treatment based on tumor volume [4]: a complete, partial, stable, and progressive disease. In 2000, the Response Evaluation Criteria for Solid Tumors (RECIST) proposed to sum one-dimensional measurements of the greatest length of all lesions extracted from X-ray tomography (CT) or magnetic resonance imaging (MRI) images [5]. The RECIST criteria have periodically been revised, and new versions have emerged to accommodate new targeted therapies. In 2009, the Positron Emission Tomography (PET) Response Criteria for Solid Tumours (PERCIST) was introduced to provide a continuous variable for categorizing patient response to treatment. This involves calculating the percentage change between pre-and post-treatment PET scans of the peak standard uptake value (SUL) corrected for body mass or the sum of all SULs of all lesions. The RECIST and PERCIST criteria provide classification labels that respond to the macroscopic characteristics of tumors and are robust and convenient for clinical practice. However, they provide little, if any, information about the effect of a precision treatment on its pharmacological target, e.g., immune checkpoint inhibition, anti-angiogenesis, and targeted immunotherapy. Therefore, RECIST and PERCIST are of limited interest for the evaluation of new treatments, which contrasts with the increasing availability of *in vivo* molecular and functional imaging approaches targeting tumor hallmarks [6], and even the interaction of these hallmarks through hybrid imaging [7–9]. Thus, new tumor response criteria specific to the pharmacological target being addressed are needed.

Artificial intelligence (AI), a term derived from the informatics field, has shown promising potential to accelerate the evolution of healthcare toward precision oncology [3,10]. In particular, machine learning (ML), a branch of AI that applies statistical methods to detect patterns within datasets, enables the assembly and analysis of large volumes of data and facilitates diagnosis, prognosis, and treatment response assessment [3,10–18]. Traditionally, unsupervised ML clustering methods have been used to cluster the molecular and/or genomics patient profiles and to analyze in response to treatment [18] with posterior supervised learning generalization [19]. These early “omics” studies have laid the groundwork for more recent analyses using profiles created with radiology imaging features, known as radiomics. Radiomics provide a large number of quantitative features that can be used by ML methods to detect high-dimensional patterns that correlate with relevant clinical endpoints. Because they can be applied to routinely acquired images at no cost, radiomics have expanded to almost all branches of molecular imaging [20–22], anatomical imaging [23–25] and hybrid imaging [12]. However, radiomics techniques possess several limitations. Firstly, the biological significance of the imaging features extracted through radiomics is often unclear. To overcome this limitation, certain studies have attempted to establish correlations between radiomics features and manually crafted biological descriptors derived from the images [17]. However, numerous radiomics features remain inadequately understood and their clinical applicability is hampered by a lack of interpretability [26,27]. Secondly, radiomics involves a vast number of features computed using predefined mathematical expressions [12]. Given that translational research datasets are often limited in size, it is probable that employing numerous features may result in overfitting during machine learning (ML) training [28]. Therefore, most radiomics studies concentrate on large clinical databases. On the other hand, preclinical studies, which, due to animal experimentation regulations, rely on small databases, often favor the use of a few handcrafted clinical image descriptors with direct biological interpretation [29].

In this study, we investigate the response to an antitumoral treatment of paragangliomas (PGLs), rare neuroendocrine tumors arising from extra-adrenal chromaffin cells

that originate from the neural crest cells and are characterized by high metabolism and extensive vascularization [30]. Sunitinib is an anti-angiogenic drug used to treat patients with PGLs [31]. In previous work by our team, we showed that the response to sunitinib treatment in experimental PGLs-bearing mice was highly variable [32]. In some animals, the tumors responded well to sunitinib, while in other animals, the tumors resumed growth in just a couple of weeks [32]. During treatment, we documented the vascular (using ultrafast Doppler imaging (UDI)), metabolic (using PET), and anatomical (using CT) responses of mice to sunitinib using a new hybrid imaging system that combines PET-registered ultrafast sonography (PETRUS) [33]. Imaging with PETRUS sunitinib-treated or sham-treated mice documented the effect of sunitinib on tumor growth, vessels development, and $2'$ - $[^{18}\text{F}]$ fluoro- $2'$ deoxy-D-glucose (FDG) uptake [32].

Here, we combine hierarchical clustering analysis (HCA) and supervised ML classifiers to identify different stages of tumor progression and the response of PGLs undergoing sunitinib or sham treatments using a few longitudinal-handcrafted vascular–molecular–anatomical features with direct biological interpretation. Multiple classical ML classifiers exist with simplified models suitable for small preclinical databases such as ours, and to date, it has not been explored which classifier is best suited to the task of identifying response to the sunitinib treatment of PGL using multimodal descriptors. Therefore, in this work, we evaluated several ML classifiers and used the one with the best performance for the generalized classification of tumor progression stages. The concatenation of the resulting stages along the duration of anti-angiogenic or sham treatments resulted in the identification of trajectories of tumor evolution.

2. Materials and Methods

Figure 1 shows the pipeline of the framework implemented in this study that progresses from the acquisition of multi-modal image volumes to the definition of individual trajectories of response to treatment. Each element of this diagram will be described in the following sections.

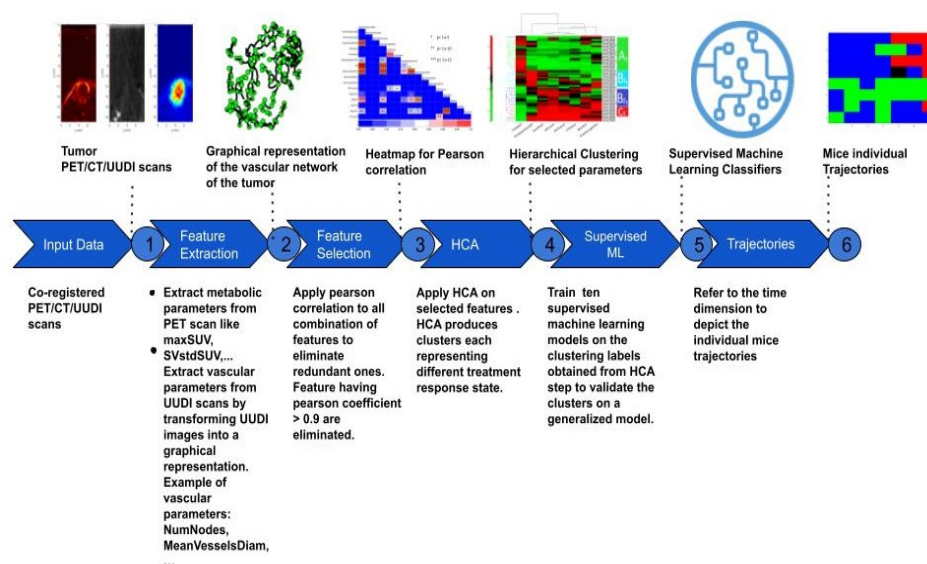


Figure 1. Process diagram showing the framework pipeline. Images were co-registered and processed to extract features describing the metabolic, vascular, and morphological components of tumor development. A Pearson correlation study was performed to remove redundant features. Longitudinal features were combined, and hierarchical clustering analysis was applied to obtain clusters and classes representing different stages of tumor evolution. The clusters and classes identified with HCA were used with 10 different supervised machine-learning classifiers for model generalization and final validation. Finally, time-wise concatenation of the identified stages was performed to form the individual trajectories of tumor evolution for each animal.

2.1. Acquisition of Live Animal IMAGING Data

Two groups of mice followed the protocol of animal housing, tumor implantation, follow-up, and anti-angiogenic drug delivery described in [32] and schematized in Figure 2. The first group (training group) included 16 mice from [32], while the second group (validation group) included another 11 mice that underwent the same experimental protocol. Imaging of the training group was performed at baseline, and then every week until week 3 for vehicle-treated animals (8 mice), and every week until week 6 for sunitinib-treated animals (8 mice). The validation group concerned only sunitinib-treated animals, and imaging was performed at the baseline, week 1, week 3 and week 6.

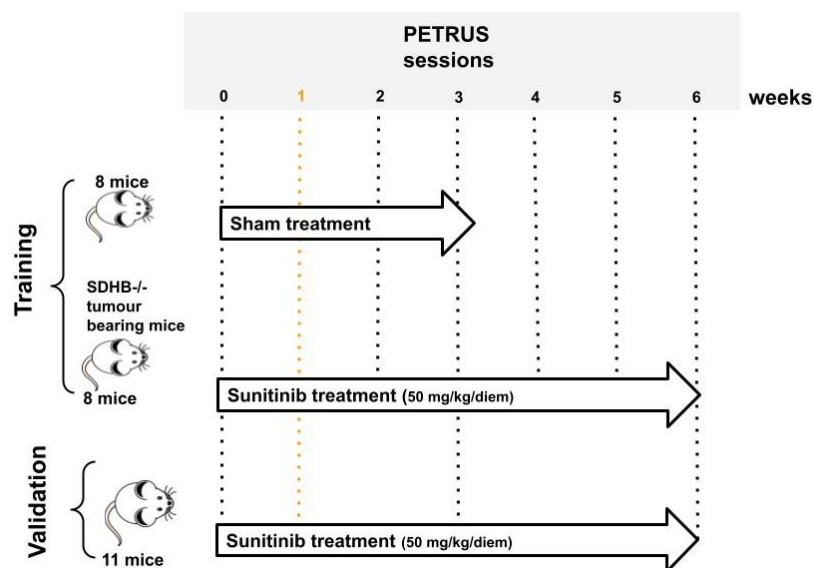


Figure 2. Database generation process. Mice in the training group were divided into two groups: sunitinib-treated and sham-treated. Eight mice from each group were scanned with PETRUS before and after 1, 2, and 3 weeks of treatment. Sunitinib-treated mice were also imaged at 4, 5, and 6 weeks of treatment. Mice of the independent validation set were sunitinib-treated and scanned at baseline and at weeks: 1, 3, and 6 of the treatment.

Animal experiments were approved by the French Ethical committee under reference No. 16-098 and performed by certified personnel following the French law on animal experimentation n°2013-118. In brief, adult female nude 6-week-old mice weighing 30 g (Janvier Labs, France) were implanted in the dorsal fat pad with tumors obtained from immortalized mouse chromaffin cells (imCC) carrying a homozygous knockout of the *Sdhd* gene (*Sdhd*^{-/-}) as previously described [32]. Mice were housed under controlled temperature (24 °C), relative humidity (50%), a 12/12 light/dark cycle, and free access to water and food. When the tumor volume reached 140 mm³, mice were randomly divided into a vehicle group (CON, *n* = 8) and a sunitinib group (SUNI, *n* = 8). The sunitinib group received sunitinib malate (Clinisciences, A10880-500) daily at a dose of 50 mg/kg body weight for 6 consecutive weeks, administered by oral gavage of 200 µL in a 10 mg/mL DMSO/PBS (1:4) solution. The control group received daily 200 µL doses of the DMSO-PBS solution (1:4) for 3 weeks. Mice were euthanized if the tumor volume exceeded UKCCCR recommendations [34] or if they showed signs of advanced cancer disease.

The effect of sunitinib was monitored non-invasively using the hybrid In vivo imaging technology PETRUS (positron emission tomography registered ultrafast sonography) [33], which allows for the simultaneous acquisition of tissue metabolism using [¹⁸F]Fluorodeoxyglucose (FDG) PET, computed tomography (CT) and ultrafast ultrasound Doppler imaging (UUDI) [33]. PETRUS simultaneously reads the cellular metabolism activity alongside the micro-vascular architecture within the tumor, ensuring unimpaired physiological conditions for both sets of spatially co-registered features [32].

2.2. Description of Database Formation

Each PETRUS acquisition comprised three image volumes registered in a common time and space reference frame that defined a multiparametric cube surrounding the animal tumor. The features describing the metabolic, vascular, and anatomical characteristics of the tumor were extracted from the PET, UUDI, and CT images, respectively (Table 1). A volume of interest (VOI) covering the whole tumor was defined on the PET images by segmenting voxels with an FDG standard uptake value (SUV) greater than 30% of the tumor's peak SUV at 50–60 min post-injection [35]. This VOI was used to create a binary mask that was applied to the three spatiotemporal registered volumes. From the masked PET image, the following metabolic features were extracted: mean, coefficient of variance, minimum and maximum of standard uptake values (MeanSUV, CVstdSUV, MinSUV, MaxSuv), and PET volume (PETVolume). The masked UUDI volume was filtered using a Hessian-based vessel enhancement filter, and vessels were segmented using predefined thresholds [36] and skeletonized using an iterative ordered thinning-based skeletonization method [37,38]. The skeletonized mask of vessels was transformed into a graph of nodes and edges representing the vascular network of the tumor. Using this graph, the following features describing the topology of the tumor vascularization were calculated: mean, minimum and maximum vessel length (MeanVesselsLength, MinVesselsLength, MaxVesselsLength), mean vessels tortuosity (Tort), which is the shortest distance between nodes divided by the vessel length), vessels length dispersion (VesselsLength-Disp), which is the standard deviation of the vessels length divided by the mean of the vessels length, number of nodes (NumNodes), density of nodes (DensityNodesinUSV), mean vessels diameter (MeanVesselsDiam) and ultrasound volume (USVolume), which is the number of voxels of the vascular skeleton multiplied by the voxel volume. The quantification of PETRUS images was performed using MATLAB version R2021b. The CT volume (CTVolume) was delineated from the fat pad surrounding the tumor.

Table 1. PET/CT/UUDI extracted features.

Parameter	Modality	Abbreviation	Unit	Description
Mean Standardized Uptake Value	PET	Mean SUV	a.u.	Average of the Standardized Uptake of FDG in the VOI
Max Standardized Uptake Value	PET	Max SUV	a.u.	Average of the 5 hottest pixels in the tumor VOI
Min Standardized Uptake Value	PET	Min SUV	a.u.	Minimum Standard Uptake of FDG in the VOI
Standardized Uptake Value of FDG dispersion	PET	CVstdSUV	a.u.	Coefficient of variance of the Standardized Uptake Value
PET volume	PET	PETvolume	mm ³	Number of voxels in the VOI × volume of a voxel
Computed Tomography Volume	CT	CTVolume	mm ³	Tumor volume defined by the CT scan
Number of Nodes	UUDI	NumNodes	nodes	Sum of all Nodes.
Number of Nodes/Vessels Volume	UUDI	DensityNodesinUSV	nodes/mm ³	Number of nodes per unit of vessel volume.
Maximum Vessels Length	UUDI	MaxVesselsLength	mm	Average of the maximum length of all the vessels
Mean Vessels Length	UUDI	MeanVesselsLength	mm	Average of the length of all the vessels
Minimum Vessels Length	UUDI	MinVesselsLength	mm	Average of the min length of all the vessels
Length Vessels Dispersion	UUDI	VesselsLengthDisp	a.u.	Coefficient of variance of the mean vessel length
Mean Vessels Tortuosity	UUDI	Tort	a.u.	Average of all tortuosities. The tortuosity is the ratio between the length of a vessel (as an arc) and the straight-line length between its initial and final points
Mean Vessels Diameter	UUDI	MeanVesselsDiam	mm	Average of all mean Diameter
Vessels Volume	UUDI	USVolume	mm ³	Tumor blood volume defined by the Ultrasound Doppler scan

The working database assembled all 15 features extracted from the imaging modalities, as well as a unique record number that defined the mouse, the week of the imaging session (where week zero (W0) is the pre-treatment imaging session and W1-6 is the rest of the treatment weeks), and the treatment group assignment (CON for sham-treated mice; SUNI for sunitinib-treated mice). Data were divided into 3 subgroups, (i) $D_{training}^{suni}$ containing the SUNI mice in the training group, aggregating a total of 54 records (ii) $D_{training}^{con}$ containing the CON mice from the training group, forming a total of 27 records, and (iii) $D_{validation}^{suni}$ containing the SUNI mice from the validation group forming a total of 28 records.

2.3. Feature Selection

Feature selection is an important pre-processing step that affects the accuracy and decreases the training time of any classifier. By removing non-useful or redundant features, the dimensionality of the feature space can be reduced, an essential step to improve the performance of a classifier [39]. In order to identify linear correlations between the different features, we applied a Pearson correlation using a Pearson coefficient $|r| > 0.9$ (p -value < 0.05) to detect redundant features [40]. In addition, non-informative features with a low coefficient of variation ($CV < 0.1$) were removed.

2.4. Unsupervised Classification: Hierarchical Clustering

One of the fundamental objectives of our study was the determination of phenotypically representative clusters, each cluster being a representative combination of metabolic, anatomical and vascular features associated with a stage of response to sunitinib. Clusters were determined by the individual response of the subject, independently of the time of treatment by assembling all the longitudinal features extracted. HCA, an unsupervised machine-learning clustering approach [41], was used to stratify the tumor response by finding common metabolic, anatomical and vascular phenotypic patterns of the image descriptors selected. The HCA was applied on each of the training datasets separately, $D_{training}^{suni}$ and $D_{training}^{con}$, in order to determine whether or not the treatment changes the time course of tumor evolution. First, the input data were standardized using the z-score. Then, the interrelationship between individual records was measured by computing the unweighted average Euclidean distance. This was followed by computing the average link as a similarity metric to define the closest pair of clusters. Finally, a heat map with dendrograms was constructed to display the patterns observed and the clusters identified. The length of the dendrogram branches connecting records and features is inversely proportional to the similarity of their profiles. Gap statistics [42] was applied in order to evaluate the optimal number of clusters, and Welch's t -test was applied to identify significantly different clusters [43]. The outcome of this analysis provided the optimal number of clusters corresponding to a particular phenotype identified for each instance in the data-base. HCA and statistical tests were implemented in MATLAB (version 2021-b) using the `clustergram`, `ttest2`, and `evalclusters` functions, respectively.

2.5. Supervised Classification: Model Building and Validation

To test the stability of the method, we compared the clustering results applied on an external population ($D_{validation}^{suni}$) to a classification produced as a generalization of the clustering performed on our initial population ($D_{training}^{suni}$). More precisely, we considered the clusters of the initial population ($D_{training}^{suni}$) as classes of a supervised classification algorithm to predict the classes expected in the new population ($D_{validation}^{suni}$).

Because our training dataset has an unbalanced number of instances per class, which can undermine the predictability of the models, we performed oversampling through the synthetic minority over-sampling technique (SMOTE), which balances the minority classes [44]. This technique uses the k-nearest neighbors approach to synthesize new observations based on the existing records. We applied smote using the four nearest neighbors to balance each of the four clusters (A, B1, B2, and C).

The selected features of our $D_{training}^{suni}$ were brought into ten machine learning classifiers, including decision tree (DT), Gaussian naive Bayes (GNB), kernel naive Bayes (KNB), linear support vector machine (Linear SVM), quadratic support vector machine (Quadratic SVM), k-nearest neighbors (KNN), weighted k-nearest neighbors (Weighted KNN), random forest (RF), narrow neural network (Narrow NN), bilayered neural network (Bilayered NN). The best-performing model was selected by comparing the area under the receiver operating characteristic curve (AUC) and accuracy (ACC) values. The control parameters of the best model were further optimized by Bayesian optimization and five-fold cross-validation to evaluate the performance of the classifier. All classifiers were trained and validated using the *classification learner* application implemented in MATLAB version 2021-b.

In order to check the relative importance of each of the metabolic, vascular, and morphological features in the classification problem, we used the predictor importance attribute associated with the RF model. The predictor importance attribute is an implicit technique performed using the RF model and is evaluated using the Gini impurity criterion index. This index is based on the principle of impurity reduction to provide the power of each feature in the classification [45].

2.6. Identification of Trajectories of Treatment Responses

We then tested whether the records assembled within each cluster, corresponding to a tumor state with specific biomarkers, could represent a chronological stage of tumor evolution. By referring back to the time point of each record (the week after the beginning of treatment) in both the CON and SUNI groups, the clusters were ordered chronologically, and a time-dependent trajectory was obtained for each mouse. We applied an R^2 test to the states at each of the seven time points of the study (classes obtained from the HCA, considering A = 1, B1 = 2, B2 = 3, and C = 4) to determine if these states indicated temporal stages of treatment response. Finally, the transitional matrix between clusters was analyzed.

3. Results

3.1. Pearson Correlation

Figure 3 shows the cross-heatmap of the Pearson correlation values (r) of CT, vascular, and metabolic features. In order to eliminate redundant features, a Pearson significance of $r > 0.9$ and p -value < 0.05 were applied to all pairs of features of the four instances. This reduced the number of vascular features from 11 to 8: MeanVesselsLength was correlated with MeanVesselsDiameter, Tort, and VesselsLengthDisp; VesselsLengthDisp correlated with MeanVesselsDiameter and Tort, and Tort correlated with MeanVesselsDiameter. Hence, MeanVesselsLength, MeanVesselsDiameter and Tort were not considered further. Applying the same Pearson r and p values reduced the metabolic features from 5 to 4: MeanSuv correlated with MaxSuv, and MaxSuv was not considered further.

With respect to vascular–metabolic correlations, interestingly, the StdSUV was significantly correlated with MeanVesselsDiam and MeanVesselsLength.

In addition, a low coefficient of variation ($CV < 0.1$) results in a non-informative dataset from classifiers' training. Thus, features having a high Pearson correlation and a low coefficient of variation were not considered further. Overall, 8 features, including 4 vascular features, i.e., USVolume, NumNodes, DensityNodesinUSV, VesselsLengthDisp, 3 metabolic features, i.e., StdSUV, PETVolume, MeanSUV, and the CT volume, were used for all three curated databases ($D_{training}^{suni}$, $D_{training}^{con}$, $D_{validat}^{suni}$).

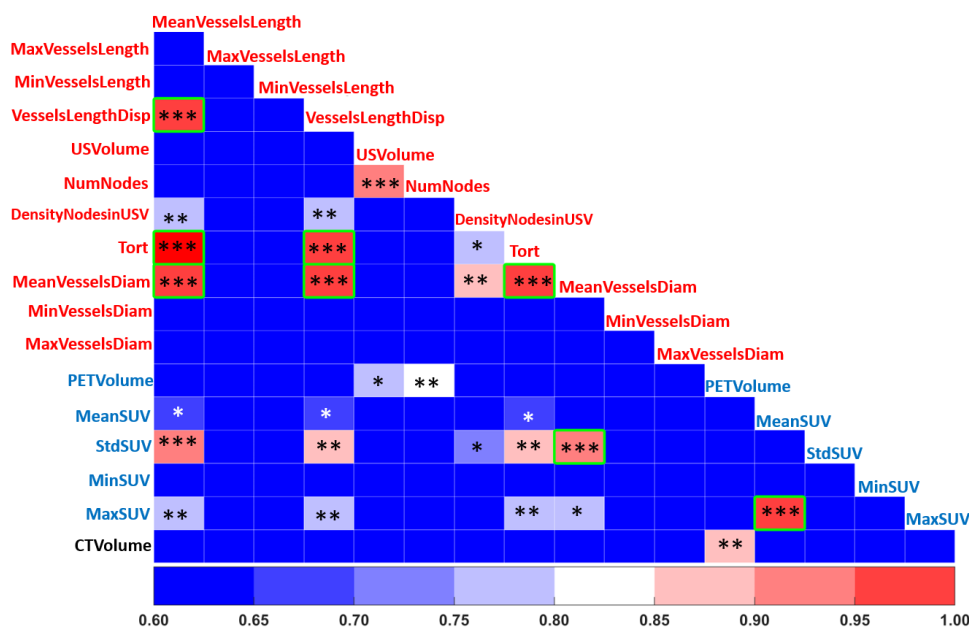


Figure 3. Heatmap summarizing significant Pearson coefficient values for each pair of metabolic (blue font), vascular (red font) and morphological features (black font) used to exclude redundant features (*, **, ***, refer to *p*-value level of significance).

3.2. Hierarchical Clustering Approach

3.2.1. Sham-Treated Training Set ($D_{training}^{con}$)

Performing the hierarchical clustering on the $D_{training}^{con}$ dataset identified two major clusters: Clusters A_c and C_c (Figure 4a), where subscript c stands for the control group. They showed the following characteristics (Table 2):

- Cluster A_c was characterized by significantly low volumes of CT, PET, and UUDI, a high coefficient variance of the standard deviation of SUV, a low number of nodes, and a low density of nodes. This corresponds to a small-sized tumor, with low vascularization and metabolism, and a heterogeneous distribution of FDG uptake.
- Cluster C_c was characterized by high volumes of CT, PET, and UUDI, a significantly lower coefficient of variation of the standard deviation of SUV, and a high number of nodes. This cluster corresponds to a stage where the tumor has grown to a large volume, with high metabolic and vascularization activities but a low heterogeneity in the distribution of FDG uptake.

Table 2. Metabolic, vascular, and morphological characteristics of the clusters of the $D_{training}^{con}$ dataset. The average values of each parameter of each cluster are represented. In black, the mean values; in parenthesis, the standard mean errors; and in blue, the z-score means.

Features	CVstd-SUV	Density Nodes inUSV (1/mm ³)	Num-Nodes	US Volume (mm ³)	PET Volume (mm ³)	CT Volume (mm ³)	Mean SUV	Vessels Length Disp (mm ²)
Cluster A_c	45.07 (1.68), 0.42	36.27 (1.85), −0.27	542.85 (32.84), −0.81	15.31 (1.02), 0.82	236.43 (27.75), −0.85	165.06 (23.80), −0.85	1.96 (0.10), −0.63	60.06 (1.89), 0.00
Cluster C_c	35.74 (0.89), 0.42	38.79 (1.57), −0.27	1549.29 (123.44), −0.81	39.44 (2.50), 0.82	815.28 (69.49), −0.85	584.29 (51.77), −0.85	2.66 (0.08), −0.63	59.60 (1.19), 0.00

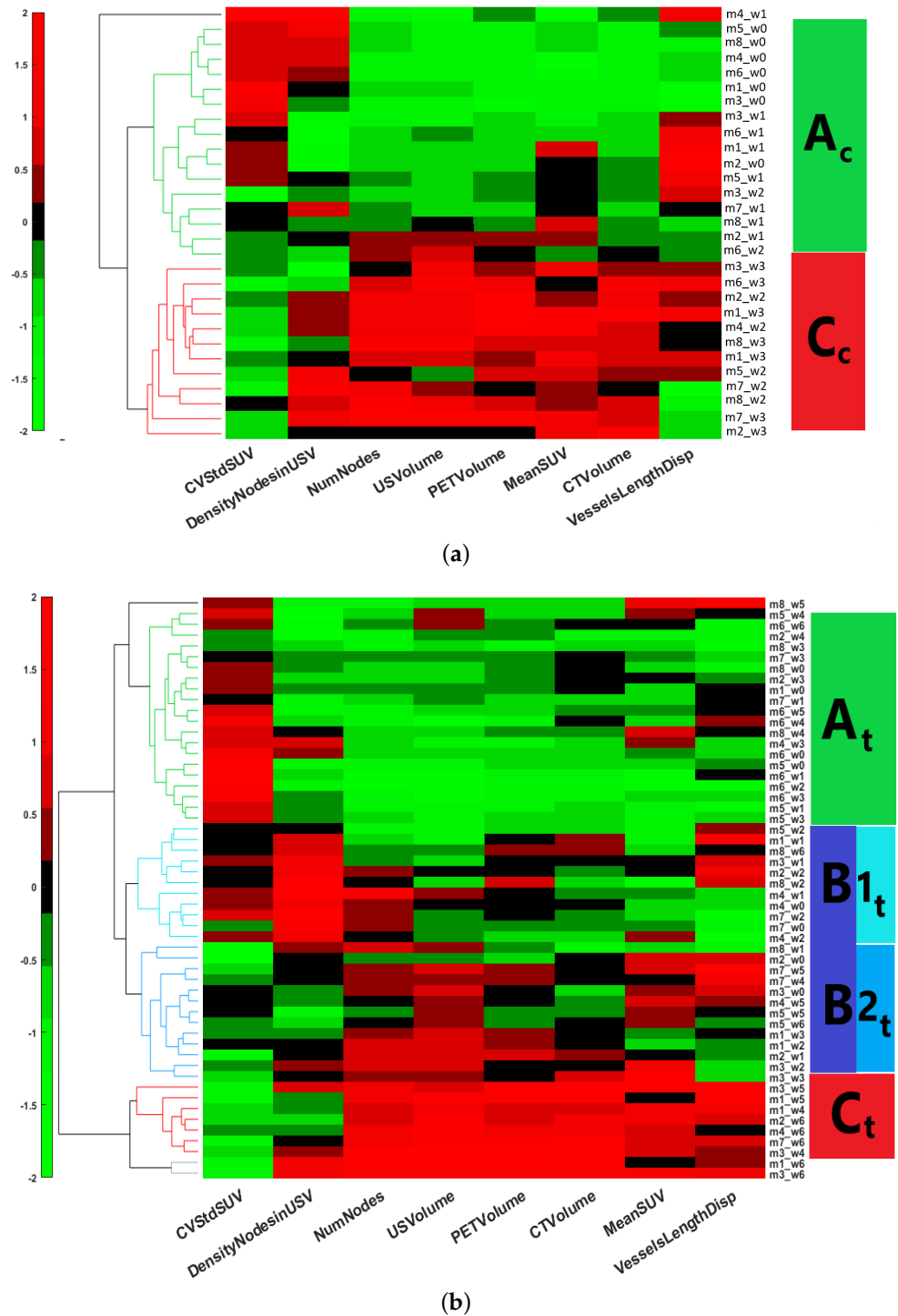


Figure 4. Heatmap and hierarchical clustering performed (a) on the $D_{training}^{con}$ dataset and (b) on the $D_{training}^{sun_i}$ dataset. Two clusters (A_c, C_c) were identified in (a) and 4 clusters ($A_t, B1_t, B2_t,$ and C_t) were identified in (b).

3.2.2. Sunitinib-Treated Training Set ($D_{training}^{sun_i}$)

The same clustering approach applied to the $D_{training}^{sun_i}$ dataset identified three major clusters (Figure 4b): Clusters $A_t, B_t,$ and C_t , where the subscript t stands for the treatment group. Cluster B_t splitted into two subgroups: $B1_t$ and $B2_t$ (Table 3).

- Cluster A_t was characterized by low volumes of CT, PET, and UUDI, a high coefficient of variation of the standard deviation of SUV, and low vessel length dispersion,

number of nodes, and density of nodes. This corresponds to a small-sized tumor with low vascularization and heterogeneous distribution of FDG uptake value, features that are similar to those of cluster A_c of the control group.

- Cluster C_t was characterized by high volumes of CT, PET, and UUDI, low coefficient of variation of the standard deviation of SUV, high vessel length dispersion, and very high number of nodes. This cluster corresponds to a tumor with a large volume, high metabolism and vascularization, and low heterogeneity in the distribution of FDG uptake, features that are similar to those of cluster C_c of the control group.

To compare the A and C clusters obtained with the SUNI and CON groups, respectively, a Kruskal–Wallis test [46] was performed between the A_t and A_c clusters, and also between the C_t and C_c clusters. The clusters were statistically similar (p -value < 0.05), indicating that clusters A_t and A_c on the one hand, and clusters C_t and C_c on the other hand, correspond to similar tumor states in the sunitinib-treated and sham-treated groups.

In the sunitinib-treated training set, the HCA algorithm identified two further clusters not present in the CON group:

- Cluster $B1_t$ was characterized by low to moderate volumes of CT, PET, and UUDI, low coefficient of variation of the standard deviation of the SUV, high vessel length dispersion, and a very high density of nodes. This corresponds to a small tumor with a significant but moderate level of vascularization, and medium-to-high heterogeneity in the distribution of FDG uptake.
- Cluster $B2_t$ was characterized by moderate volumes of CT and PET, high UUDI volume, lower coefficients of variation of the standard deviation of SUV, high vessel length dispersion, and low density of nodes. This corresponds to a moderate to high tumor volume and vascularization and low heterogeneity in the distribution of FDG uptake.

Table 3. Metabolic, vascular, and morphological characteristics of the clusters from the $D_{training}^{suni}$ dataset. The mean values of each parameter of each cluster are represented. In black, the means; in parentheses, the standard means error; and in blue, the z-score means.

Features	CVstd-SUV	Density Nodes inUSV (1/mm ³)	Num-Nodes	US Volume (mm ³)	PET Volume (mm ³)	Mean SUV	CT Volume (mm ³)	Vessels Length Disp (mm ²)
Cluster A_t	52.01 (1.17), 0.81	28.99 (1.05), −0.64	243.15 (18.20), −0.90	5.58 (0.78), −0.81	99.61 (9.73), −0.73	1.73 (0.11), −0.56	66.90 (8.22), −0.60	55.68 (0.77), −0.52
Cluster $B1_t$	47.68 (0.65), 0.12	44.08 (1.84), 1.46	527.4 (50.99), 0.16	11.84 (0.80), −0.34	195.85 (18.44), −0.09	1.79 (0.15), −0.49	100.08 (15.36), −0.29	57.33 (2.22), −0.24
Cluster $B2_t$	43.93 (0.72), −0.64	32.06 (1.02), −0.07	583.64 (29.78), 0.61	18.11 (0.46), 0.78	228.16 (15.76), 0.50	2.56 (0.22), −0.35	123.51 (11.52), 0.06	59.46 (1.40), −0.25
Cluster C_t	41.13 (0.58), −0.92	31.78 (1.29), −0.25	790.67 (39.46), 1.13	24.89 (0.73), 1.52	386.45 (29.66), 1.17	2.67 (0.12), 0.60	261.73 (17.84), 1.23	63.93 (2.01), 0.89

3.3. Robustness of Clusterization

An additional validation step was performed in order to ascertain that cluster formation was reproducible and not a casuistic process. HCA clustering was repeated on subsets of random instances of the $D_{training}^{suni}$ group, formed by randomly removing one mouse at a time. The accuracy of each HCA was calculated by considering the clusters obtained for all mice as ground truth and comparing it with the clusters of the new subset using the following formula: $Accuracy = \frac{Number\ of\ correct\ predictions}{Total\ number\ of\ Predictions}$. As shown in Table 4, the total

accuracy for each of the performed HCAs was greater than 95 percent for the three major clusters (A_t , B_t , and C_t).

Table 4. Performance of each of the HCAs for subsets of the $D_{training}^{sumi}$ dataset. Data subsets were obtained by removing all the time points of one mice at a time.

Mice Removed	1	2	3	4	5	6	7	8
Total Accuracy (%)	100	100	95	98	100	100	95	100

3.4. Performance of Supervised Machine Learning Models

All 10 of the ML classifiers explored demonstrated good predictive performance, as demonstrated by the evaluation indexes of performance presented in Figure 5a. GNB achieved the best predictive performance (AUC: 100, ACC: 98.7), whereas DT exhibited the weakest (AUC: 96, ACC: 94.8). The remaining classifiers achieved the following predicted performance: Quadratic SVM (AUC: 100, ACC: 97.4), KNB (AUC: 98, ACC: 94.8), Linear SVM (AUC: 100, ACC: 97.4), KNN (AUC: 97, ACC: 98.7), RF (AUC: 100, ACC: 94.8), Narrow NN (AUC: 100, ACC: 96.1), Bilayered NN (AUC: 98, ACC: 94.8) and Weighted KNN (AUC: 100, ACC: 97.4).

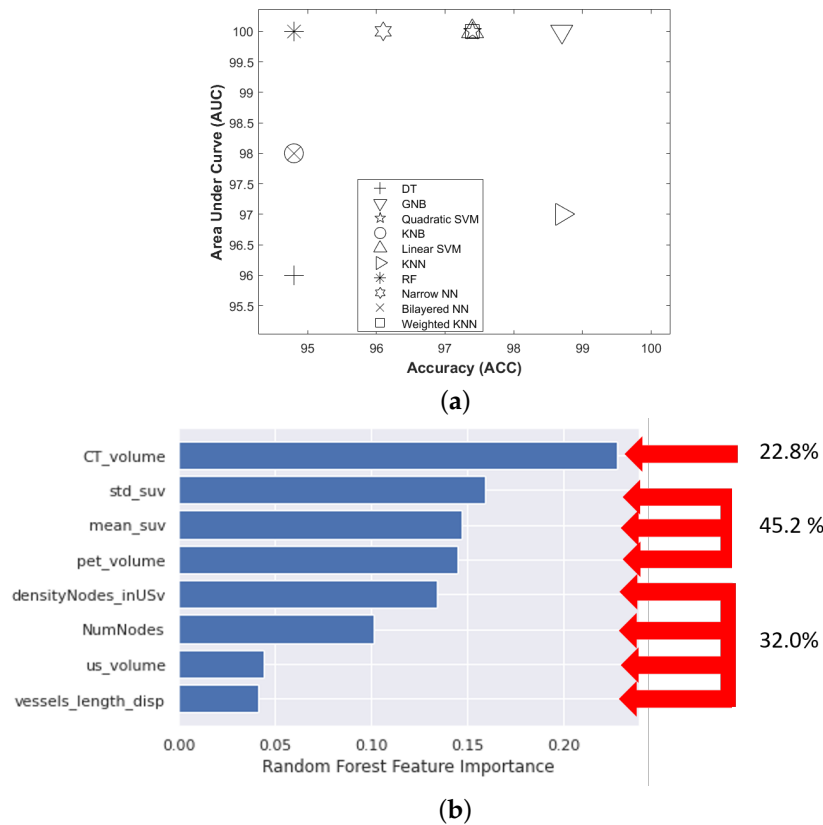


Figure 5. Performance of the supervised machine learning models (a) Scatter diagram of machine learning classifiers prediction performance. The horizontal axis represents accuracy (ACC), the vertical axis represents the area under the curve (AUC); DT, decision tree; GNB, Gaussian naive Bayes (Gaussian); Quadratic SVM, support vector machine (Quadratic); KNB, kernel naive Bayes; Linear SVM, linear support vector machine; KNN, k-nearest neighbors; RF, random forest; NNN, narrow neural network; Bilayered NN, bilayered neural network; Weighted KNN, weighted k-nearest neighbors. (b) Contribution of morphological, metabolic, and vascular features in the discrimination of the 4 clusters of tumor evolution stages identified with RF.

Applying the best classifier to the three records that had not been classified using HCA, i.e., mouse 1-week 6, mouse 3-week 6, and mouse 8-week 5, allowed to classify these

records into clusters C_t , C_t , and A_t , respectively (Table 5). This classification remained consistent with the previous stages of the sunitinib training set $D_{training}^{suni}$. The best-trained model applied to the $D_{validat}^{suni}$ dataset assigned a state for each record and mouse (Table 6) that was consistent with the states of the $D_{training}^{suni}$ dataset.

Table 5. Evolutionary path of sunitinib-treated mice of the training set. Items marked as * indicate missing classification due to the absence of corresponding PETRUS data. Clusters that were assigned by the RF model are underlined.

Mouse Number	Baseline	Week 1	Week 2	Week 3	Week 4	Week 5	Week 6
mouse 1	A_t	$B1_t$	$B2_t$	$B2_t$	C_t	C_t	C_t
mouse 2	$B2_t$	$B2_t$	$B1_t$	A_t	A_t	*	C_t
mouse 3	$B2_t$	$B1_t$	$B2_t$	$B2_t$	C_t	C_t	C_t
mouse 4	$B1_t$	$B1_t$	$B1_t$	A_t	*	$B2_t$	C_t
mouse 5	A_t	A_t	A_t	A_t	A_t	$B2_t$	$B2_t$
mouse 6	A_t	A_t	A_t	A_t	A_t	A_t	A_t
mouse 7	$B1_t$	A_t	$B1_t$	A_t	$B2_t$	$B2_t$	C_t
mouse 8	A_t	$B2_t$	$B1_t$	A_t	A_t	C_t	$B1_t$

Table 6. Clusterization of the 11 sunitinib mice from the validation group. Items marked as - indicate that the RF approach was unable to assign the record to one any of the A_t , $B1_t$, $B2_t$, C_t clusters. Items marked as * indicate no PETRUS data available.

Mouse Number	Baseline	Week 1	Week 3	Week 6
mouse 9	A_t	$B1_t$	$B1_t$	*
mouse 10	A_t	A_t	$B1_t$	C_t
mouse 11	A_t	$B1_t$	$B2_t$	*
mouse 12	A_t	$B1_t$	C_t	-
mouse 13	A_t	A_t	*	C_t
mouse 14	A_t	$B2_t$	*	*
mouse 15	$B1_t$	$B1_t$	*	*
mouse 16	$B1_t$	$B1_t$	*	*
mouse 17	A_t	A_t	$B1_t$	*
mouse 18	$B1_t$	A_t	*	*
mouse 19	A_t	*	*	*

Finally, using the RF classifier the relative importance of features used for training showed that all three types of tumor features, i.e., metabolic, vascular, and anatomical features, participated in the prediction of the four clusters (Figure 5b). This indicates that the information provided by each of the three imaging modalities contributed in a balanced way to define tumor stages for each imaging record.

Clusterization Reveals Tumor Progression

We then tested whether the different clusters would correspond to different time points during the tumor follow-up, i.e., whether, for any record, there was a correlation between assignment to one particular cluster and the time point at which imaging had been performed for that record. Regarding the CON group, all except two records (mouse 3/week 2 and mouse 6/week 2) of cluster A_c corresponded to the baseline or to the week-1 time point. Conversely, all cluster C_c records corresponded to week-2 or week-3 acquisitions. This confirms that cluster A_c represents an initial stage of the tumor, while cluster C_c represents an advanced tumor stage.

In contrast, the correspondence between the time-point of acquisition and assignment to the A_t or C_t cluster was much looser for the SUNI group than for the CON group. For example, mouse 6 remained in cluster A_t at all time points until week 6. Moreover, at baseline and week 1, a significant number of mice were not assigned to the A_t cluster but

either to the B_{1t} cluster (two mice at baseline and three at week 1) or to the B_{2t} cluster (two at each time point). Conversely, upon reaching the last observation time point (week 6), five mice from the SUNI group were in the C_t cluster, while one was classified in the B_{1t} cluster, one in the B_{2t} cluster, and one in the A_t cluster. Examples of trajectories for a mouse from the sham-treated group and for two mice from the sunitinib-treated group are shown in Figure 6a.

We then investigated the influence of the vascular and metabolic features on the clustering results. Removing PET and UUDI features from the SUNI datasets and basing clustering only on the CT volume led to the co-clustering of $[A_t;B_{1t}]$ and $[B_{1t};B_{2t}]$ (see boxplot in Figure 7a). This indicates that RECIST-like criteria using only CT did not identify intermediate clusters. When the same algorithm HCA was applied to the SUNI dataset from which the vascular features obtained by ultrasound imaging had been removed, i.e., using only the PET metabolic features and the CT volume, only two significantly different clusters were obtained using gap statistics: clusters $A_{PET/CT}$ and $B_{PET/CT}$. This indicates that PERCIST-like criteria, using PET-CT only, did not identify intermediate clusters (Figure 7b). Therefore, the intermediate B stage (B_t) and its two sub-clusters B_{1t} and B_{2t} , essentially reflect changes concerning the vascular features of tumors under sunitinib treatment.

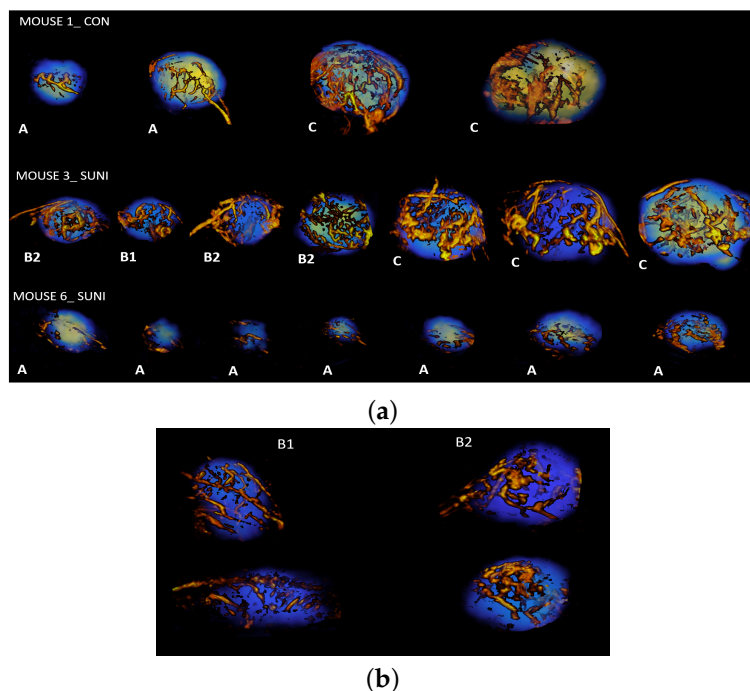


Figure 6. Maximum intensity projection renderings (MIP) of PGL tumors, (a) mouse 1 from the CON group, mouse 3 and mouse 6 from the SUNI group. Tumors in the CON group are shown at baseline and from week 1 to week 3, while tumors from the SUNI group are shown at baseline and at week 1 to week 6. (b) Comparison of PGL tumors at the B_{1t} and B_{2t} stages.

3.5. Clusters Depict Responses to Sunitinib Treatment

To further understand how clusters reflect the response to sunitinib treatment, the evolutionary trajectories (passage from one cluster to another over successive time points) were studied individually for each mouse of the SUNI group (Table 5). The progression from cluster A_t to C_t of sunitinib-treated mice was not direct as the A_c to C_c in the sham-treated animals but passed through intermediate B_t clusters. This was confirmed by a correlation analysis performed on clusters A_t , B_t and C_t considered stages 1, 2 and 3, resulting in $R^2 = 0.84$. Calculation of the cluster transition matrix confirmed the relationship between the clusters and the chronology of tumor evolution. Assuming a progression represented by states A_t , B_t , and finally C_t , we obtained 29/46 (65.9%) stable phenotypes, i.e., remaining in

the same state; 10/46 (22.7%) one progression, i.e., advancing further to the next state; and 5 (11.3%) regressions from B_t to A_t (Appendix Table A1). Pooling the validation population and the training population showed an asymmetry between “progression” ($n = 15$) and “regression” ($n = 6$). Finally, Cluster C_t was an irreversible transition deriving essentially from the B_{2t} state that appeared as a mandatory intermediate stage to reach state C_t , and the transition from B_t to A_t occurred only by the intermediary stage B_{1t} , and not by B_{2t} . States A_t , B_{1t} , B_{2t} , and C_t are thus ordered in time, suggesting that they are in fact tumor stages and that there is a progressive evolution of tumor stages from states A_t to C_t through B_t , and irreversibly between C_t and the other states.

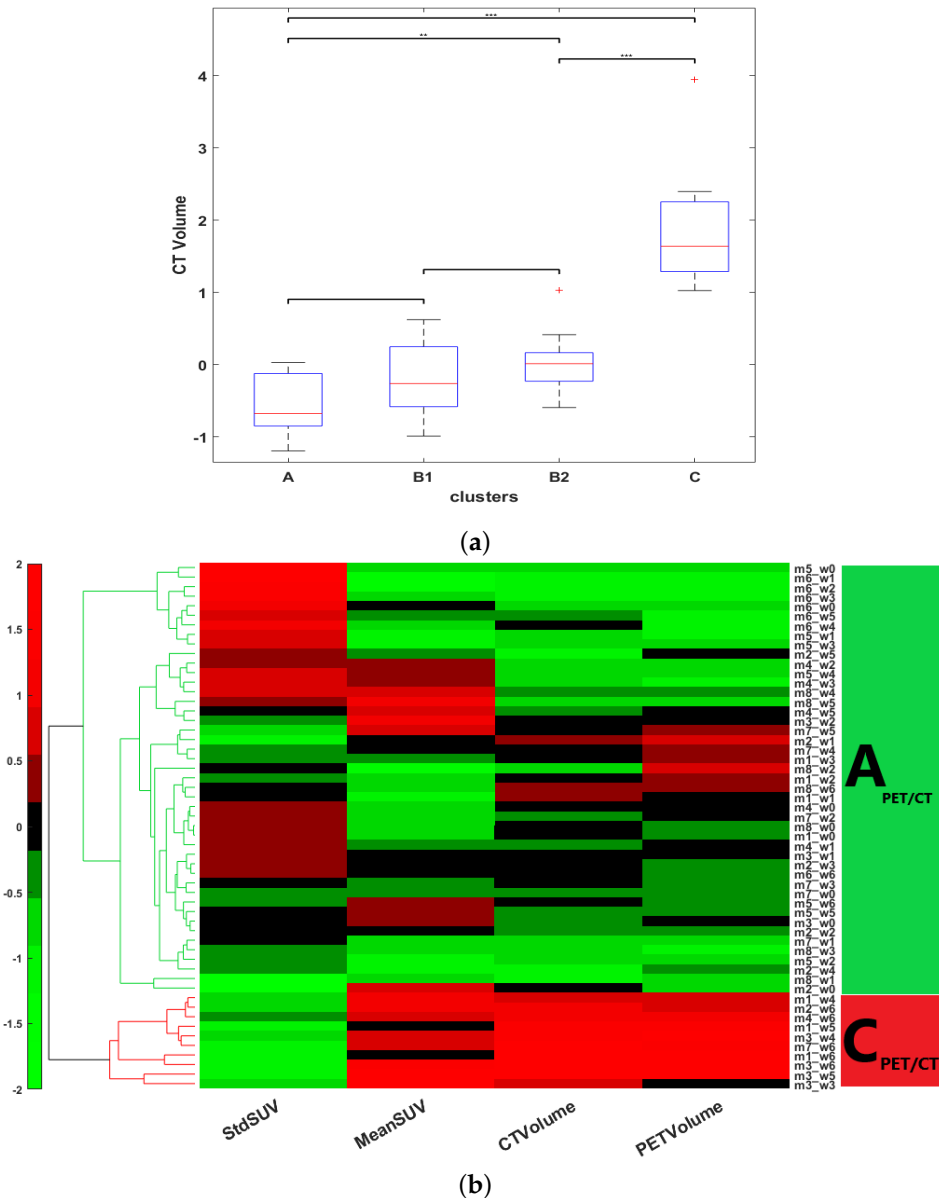
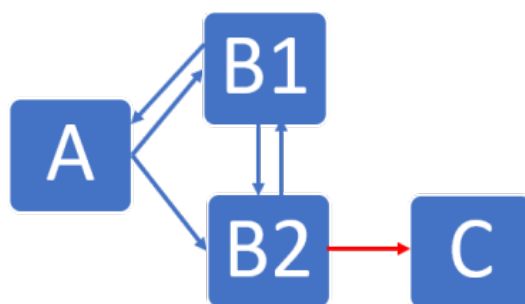


Figure 7. Contribution of the vascular features for cluster discrimination in the SUNI group (a) CTVolume shows no significant difference between A_t - B_{1t} and B_{1t} - B_{2t} ($p_value > 0.05$), indicating that RECIST criteria alone did not identify the intermediate B1 and B2 clusters. (b) Similarly, hierarchical clustering performed on the $D_{training}^{suni}$ dataset considering only the features derived from PET and CT scans did not identify the intermediate stages B_{1t} and B_{2t} either.

In summary, multi-feature ML analysis of the sunitinib-treated animals showed that individual trajectories, defined by the passage from one cluster to another, followed a discrete number of rules:

- Irrespective of whether mice received sunitinib or vehicle, no mouse reversed from the advanced tumor stage (cluster C) to a less advanced stage.
- In the sunitinib group, mice moved from the early tumor stage (cluster A_t) to either one of the two intermediate stages (clusters $B1_t$ or $B2_t$) but not directly to the advanced stage (cluster C_t).
- In the sunitinib group, mice moved from cluster $B1_t$ to $B2_t$ and back, and from cluster $B1_t$ back to cluster A_t , but no passage from cluster $B2_t$ to cluster A_t was observed.
- In the sunitinib group, all mice reaching the advanced (cluster C_t) stage originated from cluster $B2_t$.

The robust correlations between clusters and treatment duration, and the transition matrix between clusters confirm that the A, B, and C clusters correspond to tumor stages. Interestingly, transitions between sub-clusters $B1_t$ and $B2_t$ were less correlated with time than transitions between A_t and $B1_t$ or $B2_t$, and between $B2_t$ and C_t . This suggests that the “reverse” transitions, i.e., $B2_t$ to $B1_t$ and $B1_t$ to A_t , could reflect the phenotype changes associated with a positive response to sunitinib. Figure 8 summarizes the trajectories between tumor stages in sunitinib-treated mice. There was first an increase in the level of tumor vascularization (A_t to $B1_t$ transformation), followed by a decrease in the heterogeneity of FDG distribution in the tumor ($B1_t$ to $B2_t$).



cluster	volume	vascularization	FDG heterogeneity
A	Lo	Lo	Hi
B1	Lo	Med	Hi
B2	Med	Med-Hi	Lo
C	Hi	Hi	Lo

Figure 8. Graphical and tabular representations of the trajectories highlighting the major characteristic features of mice under sunitinib treatment.

4. Discussion

Previous studies used ML to study the correspondence between gene expression and tumor progression [47,48], including PGL [49]. To the best of our knowledge, this is the first application of ML based on HCA and supervised ML algorithms to noninvasive multimodal imaging of PGL. PGL lesions may concern the whole sympathetic and parasympathetic chains from the base of the skull to the pelvis. Germline mutations in one of the SDHx genes are responsible for approximately 20% of cases of PGL and also in some other tumors [50,51]. PGL patients carrying SDHx mutations show a higher rate of metastatic disease and a lower rate of survival than non-SDHx PGL patients. Surgery is not without risk and may be

impractical for numerous or misplaced lesions. Clinical trials with sunitinib have reported modest results in SDHB mutation carriers [32,52].

There is an international consensus on the use of repeated non-invasive imaging for the screening, management and follow-up of PGL patients [53], as well as for asymptomatic SDHx mutation carriers [54]. Our results show that unsupervised ML of serial noninvasive and multimodal imaging data can define the phenotypic stages of mouse *Sdhb*^{-/-} PGL tumors under anti-angiogenic treatment. The main finding is that, although the records fed to the ML algorithm had not been time stamped for the duration of treatment, unsupervised ML applied to multimodal multiparametric imaging features yielded clusters relevant to disease progression and to the response to sunitinib. In the sham-treated group, all mice switched, generally in less than three weeks, from cluster *A_c*, an early stage with small and poorly developed tumors, low vascularization, and heterogeneous FDG uptake, to cluster *C_c*, an advanced stage with large tumors, large vessels, high and relatively homogeneous FDG uptake, corresponding to an end-stage cancer disease. In the sunitinib-treated group, a given tumor from a given mouse could, over time, move from one cluster to another, suggesting that the changes from one cluster to another depicted trajectories of tumor evolution related to the response or the escape from treatment. Some sunitinib-treated tumors showed a progression similar to sham-treated tumors, which infers that sunitinib-treated mice entering the advanced-stage *C_t* cluster have escaped sunitinib treatment.

Two other clusters, *B1_t*, and *B2_t*, representing intermediate tumor stages, were observed only in the sunitinib-treated group, supporting the view that their phenotypes represent the effects of sunitinib on PGL tumors. The first one, *B1_t*, encompassed small-sized tumors with a significant but moderate level of vascularization and heterogeneity in the distribution of glucose uptake. The second cluster, *B2_t*, encompassed tumors of moderate volume and vascularization, and low heterogeneity in the distribution of glucose uptake. ML did not identify these two intermediate stages when the vascular features derived from ultrafast ultrasound were removed from the analysis. Therefore, the *B1_t* and *B2_t* intermediate stages identified the effect of sunitinib on tumor vascularization, likely by inhibition of vascular endothelial growth factors receptors (VEGFRs), the major pharmacological target of the drug [55]. Previous studies have documented the relationship between tumor vascular types and the malignancy of PGL or pheochromocytoma, which is the adrenal form of paraganglioma. In a pioneering study, Favier et al. [56] divided pheochromocytomas into two groups according to their vascular architecture. Tumors with short, straight vascular segments distributed regularly over large areas of tumoral tissue had a vascular density equivalent to that observed in the normal adrenal medulla, while tumors with longer vascular segments of irregular length and a lower density of vessels corresponded to the malignant form. These regular and irregular patterns observed using in vitro stained sections of tumor tissue samples are remarkably similar to the states that we observed here in vivo, A and C [56]. A few years later, a study attempted to use “Favier’s criteria” of the vascular patterns on histological sections of pheochromocytomas and PGL for the prediction of clinical behavior [57]. Again, malignancy was associated with an irregular vascular pattern; however, in spite of the correct agreement between observers, sensitivity and specificity were relatively modest and the authors concluded that vascular patterns, although useful, were not sufficient as “stand-alone [...] prognostic tool for the distinction between benign and malignant PCC...”. Interestingly, we observed a difference in vascular morphology reminiscent of regular/irregular patterns under sunitinib treatment, tumor vessels being larger in diameter at stage *B2_t* than at stage *B1_t* (see Figure 6b). Therefore, while the analysis of vascularization may by itself not be sufficient, and notwithstanding the fact that the morphology of vessels in fixed tissue may not reflect their in vivo morphology, there is good agreement with changes in vessel morphology and the response to sunitinib, suggesting that the in vivo exploration of vascular morphology may be useful for the management of PGL. In addition, the link between FDG heterogeneity and microvascular density was theorized using a spatiotemporal computational model [58]. Our present results are in agreement with the authors’ conclusion that “as microvascular

densities increase [...], the spatiotemporal distribution of total FDG uptake by tumor tissue changes towards a more homogenous distribution [58]". Therefore, combined imaging of vascularization and metabolism could be an advantage for the follow-up of PGL patients under treatment.

Interestingly, all of the three mice that pertained to a B cluster ($B1_t$ or $B2_t$) at baseline ended up in the C_t cluster at the end of the 6-week sunitinib treatment, while only one of the four mice pertaining to the A_t cluster at baseline ended up in the C_t cluster. Although further studies are necessary to determine whether the tumor's biology prior to the administration of sunitinib could predict future escape from treatment, this may indicate that tumors that have already developed a significant vessel network are less prone to respond to sunitinib therapy. Thus, even though the switch from $B1_t$ to $B2_t$ was reversible under sunitinib treatment ($B1_t$ to $B2_t$), increased vascularization and decreased metabolic heterogeneity defining the $B2_t$ stage were necessary features for passage to the C_t stage, in other words, for escape from sunitinib treatment. From a cancer biology point of view, this suggests that escape from sunitinib treatment involves both a metabolic and a vascular switch.

From a statistical point of view, the analysis of each record independently without time stamping allows to extraction of information regarding the rates of tumor evolution in a small group of eight mice. This would not have been possible with conventional methods based on time-stamped groups of individuals unless the number of individuals would have been drastically increased. Considering the necessity to reduce the use of animals in research, the unsupervised method for the analysis of multimodal imaging presented here is an attractive alternative for the preclinical exploration of treatments in cancer models.

Moreover, cluster extraction using multiple features could allow gaining a better understanding of the sequence of events underlying drug response. The fact that cancer is a multiform disease with multiple intermingled hallmarks has been extensively documented and reviewed in the classical paper by Hanahan and Weinberg [59]. Therefore, it is unlikely that assessing only one biomarker, even one that informs on the activity toward the pharmacological target, may be sufficient to assess treatment response, and, even less so, to identify complex escape mechanisms. All in all, our results support the recourse to multimodal imaging with the careful selection of relevant imaging biomarkers, ideally including one or several biomarker(s) of the hallmark targeted by the treatment. In this respect, other tumor variants could also benefit from similar approaches extracting biomarkers specific to the tumor type and/or treatment. Finally, it may also be interesting to apply a radiomics analysis in order to compile mathematically defined image features and determine whether they represent phenotypic states predictive of tumor stage predictive of treatment response.

The main limitation of our study is that it is based on preclinical data. Serial imaging sessions, even non-invasive, are difficult to envision in clinical settings. However, we show that comprehensive longitudinal explorations in a patient-relevant animal model can identify key imaging features leading to sunitinib resistance, and may inspire translational methods for tumor follow-up in patients. ML analysis of multimodal hybrid imaging could offer individual monitoring of the vascular and metabolic states of a tumor, thus providing valuable information for personalized treatment decisions. Our results need to be further validated on prospective cohorts and extended to the clinical situation.

5. Conclusions

The combination of hierarchical clustering and supervised machine learning algorithms provides remarkable insight into the progression of tumor development in a mouse model of paraganglioma. Through the incorporation of multi-modal information, including the vascular features of the tumor-targeted by sunitinib, our approach is successful in depicting trajectories of response to treatment. This approach could set a basis for personalized follow-up of tumors treated by targeted therapies.

Author Contributions: Conceptualization, N.M., D.B., J.L.H., B.T. and M.P.-L.; methodology, N.M., D.B., O.Z., C.F., T.Y., T.V., J.L.H., B.T. and M.P.-L.; software, N.M., and M.P.-L.; validation, N.M.; formal analysis, N.M.; investigation, N.M., D.B., O.Z., C.F., T.Y., T.V., J.L.H., B.T. and M.P.-L.; resources, N.M., D.B., O.Z., C.F., T.Y., T.V., J.L.H., B.T. and M.P.-L.; data curation, N.M. and M.P.-L.; writing—original draft preparation, N.M., D.B., O.Z., M.P.-L. and B.T.; writing—review and editing, N.M., D.B., O.Z., J.L.H., B.T. and M.P.-L.; visualization, N.M.; supervision, M.P.-L. and B.T.; project administration, M.P.-L. and B.T.; funding acquisition, N.M., M.P.-L. and B.T. All authors have read and agreed to the published version of the manuscript.

Funding: This work received funding from the Cancer Research for Personalized Medicine—CARPEM project (Site de Recherche Intégré sur le Cancer SIRIC), from the Plan Cancer Physicancer (grant C16025KS), and from the Région Ile-de-France. In vivo imaging was performed at the Life Imaging Facility of Université Paris Cité (Plateforme Imageries du Vivant - PIV), supported by France Life Imaging (grant ANR-11-INBS-0006) and Infrastructures Biologie-Santé (IBiSa). Nesrin Mansouri received a scholarship from the Ministère de l'Enseignement Supérieur et de la Recherche. This project received funding from the European Union's Horizon 2020 research and innovation program under the Marie Skłodowska-Curie Grant Agreement no. 101030046 of M. P.-L.

Institutional Review Board Statement: Animal experiments were approved by the French Ethical committee under reference No 16-098 and performed by certified personal following the French law on animal experimentation n°2013-118.

Informed Consent Statement: Not applicable.

Data Availability Statement: The data presented in this study are available in this article.

Acknowledgments: The authors thank Laure Fournier, Judith Favier, Charlotte Lussey-Lepoutre, Irène Buvat, Béatrice Berthon and J.M. Udías for rich scientific advice and discussions.

Conflicts of Interest: The authors declare no conflict of interest.

Appendix A

Table A1. Table summarizing sunitinib treatment responses. Yellow boxes correspond to tumor progression under treatment, $n = 10$ cases (22.7%), grey boxes correspond to stabilization $n = 29$ cases (65.9%), and green boxes to tumor regression $n = 5$ cases (11.3%).

	A	B1	B2	C
A	13 (29.5%)	3 (6.8%)	3 (6.8%)	0 (0.0%)
B1	5 (11.4%)	2 (4.5%)	2 (4.5%)	0 (0.0%)
B2	0 (0.0%)	3 (6.8%)	5 (11.4%)	4 (9.0%)
C	0 (0.0%)	0 (0.0%)	0 (0.0%)	4 (9.0%)

	A	B	C
A	13 (29.5%)	6 (13.6%)	0 (0.0%)
B	5 (11.4%)	12 (27.27%)	4 (9.0%)
C	0 (0.0%)	0 (0.0%)	4 (9.0%)

References

1. Tsimberidou, A.M.; Fountzilas, E.; Nikanjam, M.; Kurzrock, R. Review of precision cancer medicine: Evolution of the treatment paradigm. *Cancer Treat. Rev.* **2020**, *86*, 102019. [\[CrossRef\]](#)
2. Litjens, G.; Kooi, T.; Bejnordi, B.E.; Setio, A.A.A.; Ciompi, F.; Ghafoorian, M.; Sánchez, C.I. A survey on deep learning in medical image analysis. *Med. Image Anal.* **2017**, *42*, 60–88. [\[CrossRef\]](#) [\[PubMed\]](#)
3. Sengupta, S.; Basak, S.; Saikia, P.; Paul, S.; Tsalavoutis, V.; Atiah, F.; Peters, A. A review of deep learning with special emphasis on architectures, applications and recent trends. *Knowl. Based Syst.* **2020**, *194*, 105596. [\[CrossRef\]](#)
4. Hunter, R.; World Health Organization (WHO). *Handbook for Reporting Results of Cancer Treatment*; WHO: Geneva, Switzerland, 1979.
5. Therasse, P.; Arbuck, S.G.; Eisenhauer, E.A.; Wanders, J.; Kaplan, R.S.; Rubinstein, L.; Gwyther, S.G. New guidelines to evaluate the response to treatment in solid tumors. *J. Natl. Cancer Inst.* **2000**, *92*, 205–216. [\[CrossRef\]](#)
6. Ellenbroek, S.L.; Van Rheenen, J. Imaging hallmarks of cancer in living mice. *Nat. Rev. Cancer.* **2014**, *14*, 406–418. [\[CrossRef\]](#)

7. Kircher, M.F.; Hricak, H.; Larson, S.M. Molecular imaging for personalized cancer care. *Mol. Oncol.* **2012**, *6*, 182–195. [[CrossRef](#)] [[PubMed](#)]
8. Garg, P.K.; Deo, S.V.; Kumar, R.; Shukla, N.K.; Thulkar, S.; Gogia, A.; Mathur, S.R. Staging PET–CT scanning provides superior detection of lymph nodes and distant metastases than traditional imaging in locally advanced breast cancer. *World J. Surg.* **2016**, *40*, 2036–2042. [[CrossRef](#)]
9. Papp, L.; Spielvogel, C.P.; Rausch, I.; Hacker, M.; Beyer, T. Personalizing medicine through hybrid imaging and medical big data analysis. *Front. Phys.* **2018**, *6*, 51. [[CrossRef](#)]
10. Bertsimas, D.; Wiberg, H. Machine learning in oncology: Methods, applications, and challenges. *JCO Clin. Cancer Inform.* **2020**, *4*, 885–894. [[CrossRef](#)]
11. Tabari, A.; Chan, S.M.; Omar, O.M.F.; Iqbal, S.I.; Gee, M.S.; Daye, D. Role of Machine Learning in Precision Oncology: Applications in Gastrointestinal Cancers. *J. Cancer* **2023**, *15*, 63. [[CrossRef](#)]
12. Krajnc, D.; Spielvogel, C.P.; Grahovac, M.; Ecsedi, B.; Rasul, S.; Poetsch, N.; Papp, L. Automated data preparation for in vivo tumor characterization with machine learning. *Front. Oncol.* **2022**, *12*, 1017911. [[CrossRef](#)] [[PubMed](#)]
13. Mayerhoefer, M.E.; Materka, A.; Langa, G.; Häggström, I.; Szczypiński, P.; Gibbs, P. Introduction to radiomics. *J. Nucl. Med.* **2020**, *61*, 488–495. [[CrossRef](#)] [[PubMed](#)]
14. Bologna, M.; Corino, V.; Calareso, G.; Tenconi, C.; Alfieri, S.; Iacovelli, N.A.; Orli, E. Baseline MRI-radiomics can predict overall survival in non-endemic EBV-related nasopharyngeal carcinoma patients. *J. Cancer* **2020**, *12*, 2958. [[CrossRef](#)] [[PubMed](#)]
15. Choi, Y.S.; Ahn, S.S.; Chang, J.H.; Kang, S.G.; Kim, E.H.; Kim, S.H.; Lee, S.K. Machine learning and radiomic phenotyping of lower grade gliomas: Improving survival prediction. *Eur. Radiol.* **2020**, *30*, 3834–3842. [[CrossRef](#)] [[PubMed](#)]
16. Avanzo, M.; Stancanello, J.; El Naqa, I. Beyond imaging: The promise of radiomics. *Phys. Med.* **2017**, *38*, 122–139. [[CrossRef](#)]
17. Muller, J.; Leger, S.; Zwanenburg, A.; Suckert, T.; Lühr, A.; Beyreuther, E.; Bütof, R. Radiomics-based tumor phenotype determination based on medical imaging and tumor microenvironment in a preclinical setting. *Radiat. Oncol. J.* **2022**, *169*, 96–104. [[CrossRef](#)]
18. Ali, M.; Aittokallio, T. Machine learning and feature selection for drug response prediction in precision oncology applications. *Biophys. Rev.* **2019**, *11*, 31–39. [[CrossRef](#)]
19. Zhang, W.; Chien, J.; Yong, J.; Kuang, R. Network-based machine learning and graph theory algorithms for precision oncology. *NPJ Precis. Oncol.* **2017**, *1*, 25. [[CrossRef](#)]
20. Nioche, C.; Orhac, F.; Boughdad, S.; Reuze, S.; Soussan, M.; Robert, C.; Buvat, I. A freeware for tumor heterogeneity characterization in PET, SPECT, CT, MRI and US to accelerate advances in radiomics. *J. Nucl. Med.* **2017**, *58*, 1316.
21. Edalat-Javid, M.; Shiri, I.; Hajianfar, G.; Abdollahi, H.; Arabi, H.; Oveisi, N.; Zaidi, H. Cardiac SPECT radiomic features repeatability and reproducibility: A multi-scanner phantom study. *J. Nucl. Cardiol.* **2020**, *24*, 1–15. [[CrossRef](#)]
22. Cook, G.J.; Azad, G.; Owczarczyk, K.; Siddique, M.; Goh, V. Challenges and promises of PET radiomics. *IJROBP* **2018**, *102*, 1083–1089. [[CrossRef](#)]
23. Orhac, F.; Frouin, F.; Nioche, C.; Ayache, N.; Buvat, I. Validation of a method to compensate multicenter effects affecting CT radiomics. *Radiology* **2019**, *291*, 53–59. [[CrossRef](#)] [[PubMed](#)]
24. Schwier, M.; Van Griethuysen, J.; Vangel, M.G.; Pieper, S.; Peled, S.; Tempany, C.; Fedorov, A. Repeatability of multiparametric prostate MRI radiomics features. *Sci. Rep.* **2019**, *9*, 9441. [[CrossRef](#)] [[PubMed](#)]
25. Hu, H.T.; Wang, Z.; Huang, X.W.; Chen, S.L.; Zheng, X.; Ruan, S.M.; Kuang, M. Ultrasound-based radiomics score: A potential biomarker for the prediction of microvascular invasion in hepatocellular carcinoma. *Eur. Radiol.* **2019**, *29*, 2890–2901. [[CrossRef](#)]
26. Leijenaar, R.T.; Nalbantov, G.; Carvalho, S.; Van Elmpt, W.J.; Troost, E.G.; Boellaard, R.; Lambin, P. The effect of SUV discretization in quantitative FDG-PET Radiomics: The need for standardized methodology in tumor texture analysis. *Sci. Rep.* **2015**, *5*, 11075. [[CrossRef](#)] [[PubMed](#)]
27. Zwanenburg, A.; Vallières, M.; Abdalah, M.A.; Aerts, H.J.; Andrearczyk, V.; Apte, A.; Löck, S. The image biomarker standardization initiative: Standardized quantitative radiomics for high-throughput image-based phenotyping. *Radiology* **2020**, *295*, 328–338. [[CrossRef](#)]
28. Koh, D.M.; Papanikolaou, N.; Bick, U.; Illing, R.; Kahn, C.E., Jr.; Kalpathi-Cramer, J.; Prior, F. Artificial intelligence and machine learning in cancer imaging. *Commun. Med.* **2022**, *2*, 133. [[CrossRef](#)]
29. van Gómez, López, O.; Vicente, A.M.G.; Martínez, A.F.H.; Londoño, G.A.J.; Caicedo, C.H.V.; Atance, P.L.; Castrejón, Á.M.S. 18F-FDG-PET/CT in the assessment of pulmonary solitary nodules: Comparison of different analysis methods and risk variables in the prediction of malignancy. *Transl. Lung Cancer Res.* **2015**, *4*, 228.
30. Moog, S.; Salgues, B.; Braik-Djellas, Y.; Viel, T.; Balvay, D.; Autret, G.; Favier, J. Preclinical evaluation of targeted therapies in Sdhb-mutated tumors. *Endocr. Relat. Cancer* **2022**, *29*, 375–388. [[CrossRef](#)]
31. O’Kane, G.M.; Ezzat, S.; Joshua, A.M.; Bourdeau, I.; Leibowitz-Amit, R.; Olney, H.J.; Knox, J.J. A phase 2 trial of sunitinib in patients with progressive paraganglioma or pheochromocytoma: The SNIPP trial. *Br. J. Cancer* **2019**, *120*, 1113–1119. [[CrossRef](#)]
32. Facchin, C.; Perez-Liva, M.; Garofalakis, A.; Viel, T.; Certain, A.; Balvay, D.; Tavitian, B. Concurrent imaging of vascularization and metabolism in a mouse model of paraganglioma under anti-angiogenic treatment. *Theranostics* **2020**, *10*, 3518. [[CrossRef](#)]
33. Provost, J.; Garofalakis, A.; Sourdon, J.; Bouda, D.; Berthon, B.; Viel, T.; Tavitian, B. Simultaneous positron emission tomography and ultrafast ultrasound for hybrid molecular, anatomical and functional imaging. *Nat. Biomed. Eng.* **2018**, *2*, 85–94. [[CrossRef](#)] [[PubMed](#)]

34. Workman, P.; Balmain, A.; Hickman, J.A.; McNally, N.J.; Rohas, A.M.; Mitchison, N.A.; Straughan, D. W. UKCCCR guidelines for the welfare of animals in experimental neoplasia. *Cancer Metastasis Rev.* **1989**, *8*, 82–88. [[CrossRef](#)] [[PubMed](#)]
35. Wu, I.; Wang, H.; Huso, D.; Wahl, R.L. Optimal definition of biological tumor volume using positron emission tomography in an animal model. *EJNMMI Res.* **2015**, *5*, 1–10. [[CrossRef](#)] [[PubMed](#)]
36. Frangi, A.F.; Niessen, W.J.; Vincken, K.L.; Viergever, M.A. Multiscale vessel enhancement filtering. In Proceedings of the Medical Image Computing and Computer-Assisted Intervention—MICCAI'98: First International Conference, Cambridge, MA, USA, 11–13 October 1998; Springer: Berlin/Heidelberg, Germany, 1998; pp. 130–137.
37. Babin, D.; Pižurica, A.; Velicki, L.; Matic, V.; Galić, I.; Leventić, H.; Philips, W. Skeletonization method for vessel delineation of arteriovenous malformation. *Comput. Biol. Med.* **2018**, *93*, 93–105. [[CrossRef](#)] [[PubMed](#)]
38. Babin, D.; Pižurica, A.; De Vylder, J.; Vansteenkiste, E.; Philips, W. Brain blood vessel segmentation using line-shaped profiles. *Phys. Med. Biol.* **2013**, *58*, 8041. [[CrossRef](#)]
39. Guyon, I.; Elisseeff, A. An introduction to variable and feature selection. *J. Mach. Learn. Res.* **2003**, 1157–1182.
40. Orhac, F.; Soussan, M.; Maisonobe, J.A.; Garcia, C.A.; Verlinden, B.; Buvat, I. Tumor texture analysis in 18F-FDG PET: Relationships between texture parameters, histogram indices, standardized uptake values, metabolic volumes, and total lesion glycolysis. *J. Nucl. Med.* **2014**, *55*, 414–422. [[CrossRef](#)]
41. Müllner, D. Modern hierarchical, agglomerative clustering algorithms. *arXiv* **2011**, arXiv:1109.2378.
42. Tibshirani, R.; Walther, G.; Hastie, T. Estimating the number of clusters in a data set via the gap statistic. *J. R. Stat. Soc. Ser. B. Methodol.* **2001**, *63*, 411–423. [[CrossRef](#)]
43. Welch, B.L. The generalization of 'STUDENT'S' problem when several different population variances are involved. *Biometrika* **1947**, *34*, 28–35. [[PubMed](#)]
44. Chawla, N.V.; Bowyer, K.W.; Hall, L.O.; Kegelmeyer, W.P. SMOTE: Synthetic minority over-sampling technique. *JAIR* **2002**, *1*, 321–357. [[CrossRef](#)]
45. Strobl, C.; Boulesteix, A.L.; Zeileis, A.; Hothorn, T. Bias in random forest variable importance measures: Illustrations, sources and a solution. *BMC Bioinform.* **2007**, *8*, 25. [[CrossRef](#)] [[PubMed](#)]
46. Kruskal, W.H.; Wallis, W.A. Use of ranks in one-criterion variance analysis. *J. Am. Stat. Assoc.* **1952**, *1*, 583–621. [[CrossRef](#)]
47. Au, N.; Cheang, M.; Huntsman, D. Evaluation of immunohistochemical markers in non-small cell lung cancer by unsupervised hierarchical clustering analysis: A tissue microarray study of 284 cases and 18 markers. *J. Pathol.* **2004**, *204*, 101–109. [[CrossRef](#)]
48. Lee, S.; Jung, J.; Park, I.; Park, K.; Kim, D.S. A deep learning and similarity-based hierarchical clustering approach for pathological stage prediction of papillary renal cell carcinoma. *Comput. Struct. Biotechnol. J.* **2020**, *18*, 2639–2646. [[CrossRef](#)]
49. Colen, R.R.; Ahmed, S.; Elshafeey, N.; Karp, D.D.; Pant, S.; Subbiah, V.; Naing, A. Radiomics to predict response to pembrolizumab in patients with advanced rare cancers. *J. Clin. Oncol.* **2020**, *38*, 66. [[CrossRef](#)]
50. Lenders, J.W.; Duh, Q.Y.; Eisenhofer, G.; Gimenez-Roqueplo, A.P.; Grebe, S.K.; Murad, M.H.; Young, W.F., Jr. Pheochromocytoma and paraganglioma: An endocrine society clinical practice guideline. *J. Clin. Endocrinol. Metab.* **2014**, *99*, 1915–1942. [[CrossRef](#)]
51. Aim, L.B.; Pigny, P.; Castro-Vega, L.J.; Buffet, A.; Amar, L.; Bertherat, J.; Burnichon, N. Targeted next-generation sequencing detects rare genetic events in pheochromocytoma and paraganglioma. *J. Med. Genet.* **2019**, *56*, 513–520.
52. Ayala-Ramirez, M.; Chougnet, C.N.; Habra, M.A.; Palmer, J.L.; Leboulleux, S.; Cabanillas, M.E.; Jimenez, C. Treatment with sunitinib for patients with progressive metastatic pheochromocytomas and sympathetic paragangliomas. *J. Clin. Endocrinol. Metab.* **2012**, *97*, 4040. [[CrossRef](#)]
53. Lloyd, S.; Obholzer, R.; Tysome, J. BSBS Consensus Group. British Skull Base Society clinical consensus document on management of head and neck paragangliomas. *Otolaryngol. Head Neck Surg.* **2020**, *163*, 400–409. [[CrossRef](#)] [[PubMed](#)]
54. Amar, L.; Pacak, K.; Steichen, O.; Akker, S.A.; Aylwin, S.J.; Baudin, E.; Lussey-Lepoutre, C. International consensus on initial screening and follow-up of asymptomatic SDHx mutation carriers. *Nat. Rev. Endocrinol.* **2021**, *17*, 435–444. [[CrossRef](#)] [[PubMed](#)]
55. Shibuya, M. Vascular endothelial growth factor (VEGF) and its receptor (VEGFR) signaling in angiogenesis: A crucial target for anti-and proangiogenic therapies. *Genes Cancer* **2011**, *2*, 1097–1105. [[CrossRef](#)]
56. Favier, J.; Plouin, P.F.; Corvol, P.; Gasc, J.M. Angiogenesis and vascular architecture in pheochromocytomas: Distinctive traits in malignant tumors. *Am. J. Clin. Pathol.* **2002**, *1*, 1235–1246. [[CrossRef](#)]
57. Oudijk, L.; Van Nederveen, F.; Badoual, C.; Tissier, F.; Tischler, A.S.; Smid, M.; Favier, J. Vascular pattern analysis for the prediction of clinical behaviour in pheochromocytomas and paragangliomas. *PLoS ONE* **2015**, *10*, e0121361. [[CrossRef](#)]
58. Kashkooli, F.M.; Abazari, M.A.; Soltani, M.; Ghazani, M.A.; Rahmim, A. A spatiotemporal multi scale computational model for FDG PET imaging at different stages of tumor growth and angiogenesis. *Sci. Rep.* **2022**, *12*, 10062. [[CrossRef](#)]
59. Hanahan, D.; Weinberg, R.A. Hallmarks of cancer: The next generation. *Cell* **2011**, *144*, 646–674. [[CrossRef](#)] [[PubMed](#)]

Disclaimer/Publisher's Note: The statements, opinions and data contained in all publications are solely those of the individual author(s) and contributor(s) and not of MDPI and/or the editor(s). MDPI and/or the editor(s) disclaim responsibility for any injury to people or property resulting from any ideas, methods, instructions or products referred to in the content.